

The fratricide of $\alpha\Omega$ dynamos by their α^2 siblings

A. Hubbard¹, M. Rheinhardt¹, and A. Brandenburg^{1,2}

¹ Nordita, AlbaNova University Center, Roslagstullsbacken 23, 10691 Stockholm, Sweden
e-mail: hubbard@nordita.org

² Department of Astronomy, Stockholm University, 10691 Stockholm, Sweden

Received 13 February 2011 / Accepted 2 September 2011

ABSTRACT

Context. Helically forced magneto-hydrodynamic shearing-sheet turbulence can support different large-scale dynamo modes, although the $\alpha\Omega$ mode is generally expected to dominate because it is the fastest growing one. In an $\alpha\Omega$ dynamo, most of the field amplification is produced by the shear. As differential rotation is an ubiquitous source of shear in astrophysics, such dynamos are believed to be the source of most astrophysical large-scale magnetic fields.

Aims. We study the stability of oscillatory migratory $\alpha\Omega$ type dynamos in turbulence simulations.

Methods. We use shearing-sheet simulations of hydromagnetic turbulence that is helically forced at a wavenumber that is about three times larger than the lowest wavenumber in the domain so that both $\alpha\Omega$ and α^2 dynamo action is possible.

Results. After initial dominance and saturation, the $\alpha\Omega$ mode is found to be destroyed by an orthogonal α^2 mode sustained by the helical turbulence alone. We show that there are at least two processes through which this transition can occur.

Conclusions. The fratricide of $\alpha\Omega$ dynamos by its α^2 sibling is discussed in the context of grand minima of stellar activity. However, the genesis of $\alpha\Omega$ dynamos from an α^2 dynamo has not yet been found.

Key words. Sun: dynamo – magnetohydrodynamics (MHD) – dynamo

1. Introduction

The observed existence of large-scale astrophysical magnetic fields, for example galactic or solar fields, is usually explained by self-excited dynamo action within electrically conducting fluids or plasmas. However, this mechanism of field amplification continues to be a matter of debate as the existing theory encounters problems when extrapolated to the large magnetic Reynolds numbers of astrophysics. Nonetheless, large-scale astrophysical fields are believed to be predominately generated by so-called $\alpha\Omega$ dynamos, in which most of the field amplification occurs through the shearing of field lines by ubiquitous differential rotation, a process known as the Ω effect (Steenbeck & Krause 1969). For example, many models of the solar dynamo invoke the strong shear found in the tachocline at the base of the convection zone (see, e.g., Charbonneau 2010). Shear alone cannot drive dynamo action however, and the α effect, caused by helical motions, provides the necessary twist of the sheared field to complete the magnetic field amplification cycle. In the Sun, an α effect is provided via kinetic helicity due to the interaction of stratified convection and solar rotation.

The α effect can drive a dynamo by itself, which is then of the so-called α^2 type. These dynamos are of great theoretical interest due to their simplicity, but are expected to be outperformed by $\alpha\Omega$ dynamos in the wild. Strictly speaking, $\alpha\Omega$ dynamos should be referred to as $\alpha^2\Omega$ dynamos as the α^2 process of course continues to occur in reality, even in the presence of the Ω effect. However, in the mean-field approach one sometimes makes the so-called “ $\alpha\Omega$ ” approximation by neglecting the production of toroidal field via the α effect entirely in favor of the Ω effect. In such models, the nonlinear competition between different $\alpha\Omega$ modes has been thoroughly studied by monitoring, for example, rapid changes of Lyapunov exponents in the bifurcation structure (Covas et al. 1997).

In the present paper we consider numerical solutions of the compressible MHD equations in three dimensions with turbulent helical flows where, of course, the $\alpha\Omega$ approximation is not applicable. Nevertheless we will refer to $\alpha\Omega$ and $\alpha^2\Omega$ regimes when shear is dominant or comparable with amplification by the helical turbulence, respectively.

Very often, a linear stability analysis of a given setup reveals that several different dynamo modes are expected to be excited at the same time. While during the linear stage the relative strength of these modes is determined by the initial conditions, the mode or mixture of modes of the final saturated state is decided by the nonlinear interactions between the modes in their backreaction on the flow. The naive guess that the final state should always be characterized by the mode with the highest growth rate, has turned out not to be valid in general. This was first shown in Brandenburg et al. (1989), who found that, for small enough dynamo numbers, the saturated state of α^2 and $\alpha\Omega$ dynamos is instead determined by the solution with the smallest marginal dynamo number. For larger dynamo numbers, however, axisymmetric dipolar and quadrupolar modes have asymptotically identical growth rates, and in the nonlinear regime there can be several stable solutions, including some with mixed parity, that no longer bifurcate from the trivial one. Moreover, certain axisymmetric solutions turned out to be unstable to non-axisymmetric perturbations and evolved eventually toward another axisymmetric solution (Rädler et al. 1990).

In direct numerical simulations of a geodynamo model with stress-free boundary conditions, it has been observed that again two different dynamo solutions, a dipolar and a “hemispherical” one, can both be stable (Christensen et al. 1999; Grote & Busse 2000). Because of the free fluid surface in that model, this might even be taken as a hint for the possibility of non-unique stable states in stellar setups as well.

Fuchs et al. (1999) have demonstrated an even more extreme case with a dynamo powered by a forced laminar flow. In the course of the magnetic field growth, the Lorentz force arranges the flow into a different pattern, which is hydrodynamically stable, but unable to drive a dynamo. As the dynamo dies out subsequently without a chance to recover, it was named “suicidal”.

Hence, the question of the character of the final, saturated stage of a dynamo cannot reliably be answered on the basis of a linear approach and the study of the nonlinear model might unveil very unexpected results. Here, we will show in a simple setup that, while $\alpha\Omega$ dynamos do grow faster than α^2 dynamos, non-linear effects are capable of driving transitions from $\alpha\Omega$ modes to α^2 modes. As the two competing dynamo modes are excited for the same parameter set, i.e., are solutions of the same eigenvalue problem, we refer to them as *fratricidal*, in reminiscence of the aforementioned suicidal dynamos.

The two astrophysical dynamos for which we have long time-series, the solar dynamo and that of the Earth, both exhibit large fluctuations. The solar dynamo in particular is known to go through prolonged quiescent phases such as the Maunder minimum (Eddy 1976). A conceivable connection with fratricidal dynamos makes understanding how non-linear effects define large-scale dynamo magnetic field strengths and geometries a matter of more than intellectual curiosity.

In Sect. 2 we sketch the mean-field theory of α^2 and $\alpha^2\Omega$ dynamos. In Sect. 3 we describe our numerical set-up and briefly discuss the test-field method, a technique to extract the turbulent transport coefficients of mean-field theory from direct numerical simulations. In Sects. 5 and 6 we describe different transition types, and we conclude in Sect. 7.

2. Mean field modeling

In the magneto-hydrodynamic approximation, the evolution of magnetic fields is controlled by the induction equation

$$\frac{\partial \mathbf{B}}{\partial t} = \nabla \times (\mathbf{U} \times \mathbf{B} - \eta \mathbf{J}), \quad (1)$$

where \mathbf{B} is the magnetic field, $\mathbf{J} = \nabla \times \mathbf{B}$ is the current density in units where the vacuum permeability is unity, and η is the microphysical resistivity. A common approach to (1) is mean-field theory, under which physical quantities (upper case) are decomposed into mean (overbars) and fluctuating (lower case) constituents:

$$\mathbf{B} = \overline{\mathbf{B}} + \mathbf{b}. \quad (2)$$

The mean can be any which obeys the Reynolds averaging rules, but is frequently assumed to be a spatial one filtering out large length-scales (a two-scale approach). Here we will however use planar averaging, either over the xy plane so that $\overline{\mathbf{B}} = \langle \mathbf{B} \rangle_{xy} \equiv \overline{\mathbf{B}}^Z(z)$ or over the yz plane, that is, $\overline{\mathbf{B}} = \langle \mathbf{B} \rangle_{yz} \equiv \overline{\mathbf{B}}^X(x)$, where $\langle \cdot \rangle_\xi$ denotes averaging over all values of the variable ξ (or volume, if not specified). A mean defined by averaging over y only will also be used ($\langle \cdot \rangle_y$). We humbly ask the reader to consider these definitions carefully, given that the two planar averages will in places be used simultaneously. It is important to remember that the superscript refers to the direction of variation, rather than the direction of averaging.

Under Reynolds averaging Eq. (1) becomes

$$\frac{\partial \overline{\mathbf{B}}}{\partial t} = \nabla \times (\overline{\mathbf{U}} \times \overline{\mathbf{B}} + \overline{\mathbf{E}} - \eta \overline{\mathbf{J}}), \quad (3)$$

$$\frac{\partial \mathbf{b}}{\partial t} = \nabla \times (\overline{\mathbf{U}} \times \mathbf{b} + \mathbf{u} \times \overline{\mathbf{B}} + \mathbf{u} \times \mathbf{b} - \overline{\mathbf{E}} - \eta \mathbf{j}), \quad (4)$$

where $\overline{\mathbf{E}} \equiv \overline{\mathbf{u} \times \mathbf{b}}$ is the mean electromotive force (EMF) associated with correlations of the fluctuating fields.

Symmetry considerations allow one to write the $\overline{\mathbf{E}}$ as a function of the mean-fields in the system. In the case of a planar averaging scheme, this relation becomes

$$\overline{E}_i = \alpha_{ij} \overline{B}_j - \eta_{ij} \overline{J}_j + \dots, \quad (5)$$

where α_{ij} and η_{ij} are turbulent transport coefficients, and averaged quantities depend on one spatial coordinate only. The traditional α effect is described by the symmetric part of the tensor α_{ij} , and requires helicity in the flow. The symmetric part of η_{ij} describes turbulent dissipation, and, in the isotropic case, appears equivalently to the microphysical resistivity η . It is therefore termed the *turbulent resistivity*, η_t . When assuming that $\overline{\mathbf{E}}$ can be completely represented by the mean magnetic field and its first spatial derivatives, the Taylor series in (5) can be truncated after the term $\eta_{ij} \overline{J}_j$. A more complete formula would include higher spatial as well as temporal derivatives.

2.1. Mean-field dynamo action

Let us assume a large-scale shearing flow of the simple form

$$\mathbf{U}_S = Sx\hat{y}, \quad (6)$$

and velocity fluctuations which are isotropic, homogeneous, and statistically stationary. Consequently, if α_{ij} and η_{ij} are assumed to be independent of $\overline{\mathbf{B}}$ (the kinematic limit), then they reduce to constant scalars α and η_t ¹.

If this system were to contain a y -dependent mean field, the shear would induce field constituents which are proportional to x . We restrict ourselves here to periodic spatial dependencies and hence exclude such unbounded fields. When identifying the y direction with the azimuthal one in a spherical system, this is equivalent to restricting to axisymmetric fields. The evolution of harmonic mean magnetic fields is given by the solution of the eigenvalue problem

$$\lambda \hat{\mathbf{B}} = \begin{bmatrix} -\eta_T k^2 & -i\alpha k_z & 0 \\ i\alpha k_z + S & -\eta_T k^2 & -i\alpha k_x \\ 0 & i\alpha k_x & -\eta_T k^2 \end{bmatrix} \hat{\mathbf{B}}, \quad (7)$$

where $\overline{\mathbf{B}} = \hat{\mathbf{B}} \exp(i\mathbf{k} \cdot \mathbf{x} + \lambda t)$, $\eta_T = \eta_t + \eta$, and $k^2 = k_x^2 + k_z^2$. The resulting dispersion relation reads

$$(\lambda + \eta_T k^2)[(\lambda + \eta_T k^2)^2 - \alpha^2 k^2 + i\alpha S k_z] = 0, \quad (8)$$

with eigenvalues (apart from the always decaying modes with $B_y = 0$)

$$\lambda_{\pm} = -\eta_T k^2 \pm (\alpha^2 k^2 - i\alpha S k_z)^{1/2}. \quad (9)$$

It can easily be seen that there are two “pure” modes with particularly simple geometries: the α^2 mode with $k_z = 0$ does not depend on S and has the form

$$\overline{\mathbf{B}}^{\alpha\alpha} = \hat{B}^{\alpha\alpha} [0, \sin k_x x, \pm \cos k_x x], \quad (10)$$

where the growth rate is $\lambda^{\alpha\alpha} = |\alpha k_x| - \eta_T k_x^2$ and $\hat{B}^{\alpha\alpha}$ is an amplitude factor. The upper (lower) sign corresponds to positive (negative) αk_x .

¹ Strictly speaking, shear could introduce anisotropy felt by mean fields with non-vanishing z -components. Our results do not reveal any such.

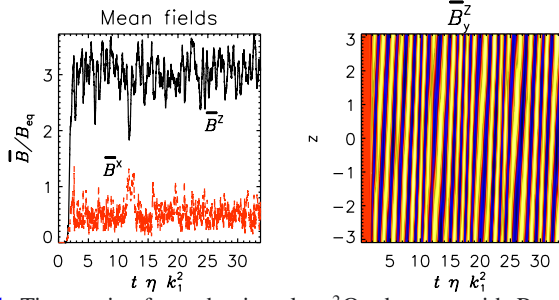


Fig. 1. Time series for a dominantly $\alpha^2\Omega$ dynamo with $\text{Re}_M = 20$, $\text{Pr}_M = 5$, $S = 0.1$ and $k_f \approx 3.1$ (corresponding to Run H of Table 3). *Left:* rms value of \bar{B}^z defined as $\langle \bar{B}^{z^2} \rangle^{1/2}$, to be associated with the $\alpha^2\Omega$ mode (black/solid), and of \bar{B}^x , defined as $\langle \bar{B}^{x^2} \rangle^{1/2}$, to be associated with the α^2 mode (red/dashed). *Right:* butterfly diagram of \bar{B}_y^z showing the dynamo wave of the $\alpha^2\Omega$ mode; yellow (blue): positive (negative) values.

In contrast, the $\alpha^2\Omega$ mode with $k_x = 0$ does depend on S and has, for $S \gg \alpha k_z$ (the $\alpha\Omega$ approximation) the form

$$\bar{B}^{\alpha\Omega} = \hat{B}^{\alpha\Omega} \left[\sin(k_z(z - ct)), \sqrt{2} \left| \frac{c}{\alpha} \right| \sin(k_z(z - ct) + \phi), 0 \right], \quad (11)$$

$$c = \text{sign}(\alpha S) \sqrt{|\alpha S / 2k_z|}. \quad (12)$$

In the above, $\hat{B}^{\alpha\Omega}$ is again an amplitude factor, ϕ represents, for $S > 0$ ($S < 0$), the $\pm\pi/4$ ($\pm 3\pi/4$) phase shift between the x and y components of the mean field, and upper (lower) signs apply for positive (negative) values of αk_z ; see Table 3 of Brandenburg & Subramanian (2005). The corresponding growth rate is

$$\Re\{\lambda^{\alpha\Omega}\} = \sqrt{|\alpha S k_z|/2} - \eta_T k_z^2. \quad (13)$$

For equal $|k|$, the $\alpha\Omega$ mode grows faster than the α^2 mode².

A key characteristic of $\alpha^2\Omega$ solutions is that the growth rate λ has a non-vanishing imaginary part $k_z c$ which results in traveling waves with phase speed c . The wave nature of $\alpha^2\Omega$ solutions is a significant draw in explaining the solar magnetic cycle. For a characteristic $\alpha^2\Omega$ dynamo found in direct numerical simulations with a setup described below, we show in Fig. 1 the time-series of rms values of \mathbf{B} alongside the traveling wave in the $z-t$ plane (“butterfly diagram”). This solution is similar to those considered recently by Käpylä & Brandenburg (2009). There are other sources for such oscillations however. Admittance of a spatially varying α enables oscillatory and hence traveling wave solutions in pure α^2 dynamos, see Baryshnikova & Shukurov (1987), Rädler & Bräuer (1987), Stefani & Gerbeth (2003), Mitra et al. (2010).

The mean fields of α^2 modes are force free, while $\alpha^2\Omega$ modes cause a potential force which has minimal effect as long as the peak Alfvén speed is subsonic so that the magnetic force cannot generate significant density perturbations. Within kinematics, the induction equation allows for superimposed α^2 and $\alpha^2\Omega$ modes. Such a superposition can extend approximately into the non-kinematic regime, and in Sect. 5 we will discuss the implications of the Lorentz forces generated when this occurs.

² When assuming both k_x and k_z to be different from zero, but keeping the $\alpha\Omega$ approximation valid and k_z fixed, the phase speed of the dynamo wave does not change while the growth rate is reduced by ηk_x^2 . However, the eigenmode has now a z component $\sim -k_x/k_z \bar{B}_x$. Such modes were not observed in our simulations.

3. Model and methods

3.1. Numerical setup

We have run simulations of helically forced sheared turbulence in homogeneous isothermal triply (shear) periodic cubic domains with sides of length 2π . The box wavenumber, which is also the wavenumber of the observed mean fields, is therefore $k_1 = 1$. Unless otherwise specified, our simulations have 64^3 grid points. For the shear flow we have taken the one defined by (6). We solve the non-dimensionalized system

$$\frac{\partial \mathbf{A}}{\partial t} = -\mathbf{U}_S \cdot \nabla \mathbf{A} - S A_y \hat{x} + \mathbf{U} \times \mathbf{B} + \eta \nabla^2 \mathbf{A}, \quad (14)$$

$$\frac{D\mathbf{U}}{Dt} = -S U_x \hat{y} - c_s^2 \nabla \ln \rho + \frac{1}{\rho} \mathbf{J} \times \mathbf{B} + \mathbf{F}_{\text{visc}} + \mathbf{f}, \quad (15)$$

$$\frac{D \ln \rho}{Dt} = -\nabla \cdot \mathbf{U}, \quad (16)$$

where \mathbf{U} is the fluid velocity excluding the shear flow, $D/Dt = \partial/\partial t + (\mathbf{U} + \mathbf{U}_S) \cdot \nabla$ is the advective derivative, $c_s = 1$ is the isothermal sound speed, ρ the density, $\mathbf{F}_{\text{visc}} = \rho^{-1} \nabla \cdot (2\rho \nu \mathbf{S})$ the viscous force, $\mathbf{S}_{ij} = \frac{1}{2}(U_{i,j} + U_{j,i}) - \frac{1}{3} \delta_{ij} \nabla \cdot \mathbf{U}$ is the rate of strain tensor, ν is the kinematic viscosity and \mathbf{f} the forcing term. We use the PENCIL CODE³, which employs sixth-order explicit finite differences in space and a third order accurate time stepping method. While our code allows full compressibility, the simulations are only weakly compressible (small Mach number). As in earlier work (Brandenburg 2001), in each time step the forcing function is a snapshot of a circularly polarized plane wave. All these waves have the same handedness, but their direction and phase change randomly from one time step to the next. This forcing provides kinetic helicity. The nondimensional forcing amplitude, f_0 (see Haugen et al. 2004, for details), is arranged such that the Mach number associated with the turbulent rms velocity is of the order of 0.1. In practice, this means that f_0 is in the range 0.02 to 0.05. The wavevectors are taken from the set of vectors that satisfy periodicity and whose moduli are adequately close to the target forcing wavenumber k_f .

The magnetic vector potential is initialized with a weak Gaussian random field, the initial velocity is given by $\mathbf{U} = \mathbf{U}_S$ and the initial density is uniform. In Table 1 we have collected the control parameters and some key derived quantities of the model. Two parameters of note are the magnetic Reynolds and Prandtl numbers,

$$\text{Re}_M = u_{\text{rms}}/\eta k_f, \quad \text{Pr}_M = \nu/\eta. \quad (17)$$

To characterize the turbulence, we provide values of α and η_t which represent the corresponding tensors as described in Sect. 2. These were determined using the test-field method (see Sect. 3.2) with test-field wavevector $\mathbf{k} = \hat{x}$ or $\mathbf{k} = \hat{z}$.

For our purposes, we require the helical turbulence to be strong enough that the α^2 dynamo can safely be excited. Accordingly, we guaranteed that in all our simulations, Re_M is above the critical value (of the order of unity) for α^2 dynamos in the corresponding *shearless* setup (Brandenburg 2009). Further, some of the transitions we will study require long simulation times due to their rarity, which constrains us to modest numerical resolutions. This in turn prevents our (explicit) numerical resistivity from being small, so the turbulent velocities must be reasonably large for the stated super-critical values of Re_M . Choosing furthermore subsonic shear speeds, we are restricted to a modest region of parameter space. In light of these limitations we operate mostly in a $\text{Pr}_M > 1$ regime.

³ <http://pencil-code.googlecode.com>

Table 1. Control and derived parameters.

Quantity	Definition	Explanation
ν	Control par.	Microphysical viscosity
η	\sim	Microphysical resistivity
S	\sim	Shear ($\mathbf{U}_S = S \mathbf{x} \hat{y}$)
f_{rms}	\sim	Forcing amplitude
k_f	\sim	Forcing wavenumber (generally ≈ 3.1)
Pr_M	ν/η	Magnetic Prandtl number
u_{rms}	$\langle \mathbf{u}^2 \rangle^{1/2}$	RMS turbulent velocity
B_{eq}	u_{rms}	Equipartition field ($\langle \rho \rangle \simeq 1$ assumed)
Re_M	$u_{\text{rms}}/\eta k_f$	Magnetic Reynolds number
k_1	$k_1 = 1$	Mean field wavenumber ($2\pi/\text{box size}$)
t_{res}	$1/\eta k_1^2$	Resistive time (mean fields)
t_{turb}	$1/u_{\text{rms}} k_f$	Turbulent time

3.2. Test-field method

A fundamental difficulty in extracting the tensors α_{ij} and η_{ij} from a numerical simulation of (14)–(16) is that (5) is under-determined. However, turbulent transport depends only on the velocity field, so “daughter” simulations of the induction equation, whose velocity fields are continuously copied from the main run, share the same tensors α_{ij} and η_{ij} . It is therefore possible to lift the degeneracy by running an adequate number of daughter simulations with suitably chosen “test” mean fields. We employ this *test-field method* (TFM); for an in-depth overview see Schrunner et al. (2005, 2007) and Brandenburg et al. (2008a,b). Recently the original method has been extended to systems with rapidly evolving mean-fields, requiring a more complicated *ansatz* than Eq. (5) (Hubbard & Brandenburg 2009) and to the situation with magnetic background turbulence (Rheinhardt & Brandenburg 2010).

In addition to calculating turbulent tensors for planar averages as described in the references above, we will be interested in tensors that depend both on x and z (that is, are y -averages). For this, we generalize (5) to

$$\bar{\mathcal{E}}_i = \alpha_{ij} \bar{B}_j + \eta_{ijk} \frac{\partial \bar{B}_j}{\partial x_k} + \dots \quad (18)$$

There are 27 tensor components (as $\partial_y \bar{\mathbf{B}} = \mathbf{0}$), so nine test-fields are required, which we choose to be of the form

$$\bar{\mathbf{B}}^{pq} = B^T f_q(x, z) \delta_{ip} \hat{e}_i, \quad p = 1, 2, 3, \quad q \in \{\text{cc}, \text{sc}, \text{cs}\}, \quad (19)$$

where $f_q(x, z)$ is defined, according to the choice of q , to be one of the following functions:

$$\cos k_1 x \cos k_1 z, \quad \sin k_1 x \cos k_1 z, \quad \cos k_1 x \sin k_1 z,$$

and B^T is, as standard for test-field methods, an arbitrary amplitude factor. Although the wavenumber of the test fields is usually treated as a varying parameter, we need here to consider only the single value k_1 because the fastest growing and also the saturated dynamos in the simulations are dominated by this wavenumber, the smallest possible in our periodic setup. As is often the case in applications of the test-field method, we will occasionally be faced with unstable solutions of the test problems. We treat that difficulty by periodically resetting the test solutions (see Hubbard et al. 2009). Since it takes a finite time for the stable parts of the test solutions to reach their stationary values, and as this time is frequently close to the required reset time, only limited windows in the time series of the data are valid.

4. Kinematic regime

The fruits of the linear analysis of Sect. 2.1 are not always clear in the kinematic regime of direct numerical simulations. Consider first a low value of $\text{Re}_M \approx 5$, slightly above its supposed marginal values for both the α^2 and the $\alpha^2\Omega$ modes. When starting with a Beltrami $\bar{\mathbf{B}}^X$ field as in (10) with $k_x = k_1$, the initialized dynamo mode indeed starts to grow exponentially after a short adjustment stage. Its corresponding sibling mode, that is, the $\alpha^2\Omega$ one, is fed via fluctuations and after a certain delay starts to grow exponentially in turn. Even without including memory effects, the estimated growth rates are in good agreement with those obtained from the transport coefficients measured by the test-field method. Further, the expected geometries of both modes can be identified satisfactorily. If instead one uses the measured transport coefficients to generate an appropriate initial $\alpha^2\Omega$ field whose geometry is described by (12) with $k_z = k_1$, it grows again at the right rate. Its α^2 sibling, however, never appears. Instead a $\bar{\mathbf{B}}^X$ field follows the $\alpha^2\Omega$ mode, albeit with an rms value one order of magnitude lower: we interpret this as “enslavement” of the $\bar{\mathbf{B}}^X$ field by the growing $\alpha^2\Omega$ mode: i.e., much like in Sect. 6.3, the magnetic field of the $\alpha^2\Omega$ mode forces $\bar{\mathbf{B}}^X$ via turbulent motions that can be represented by transport coefficients depending on both x and z . Only the geometry of the $\alpha^2\Omega$ mode can be safely identified, while the $\bar{\mathbf{B}}^X$ field shows a strong imprint of the forcing wavenumber, furthering the enslavement hypothesis.

Even for higher Re_M the kinematic picture should still be clear in the shearless case, $S = 0$: when starting with random initial conditions one expects all three (Beltrami) α^2 modes possible in a box, that is, with $|\mathbf{k}| = k_1$, to grow at similar rates. In Fig. 2 we present time series, a butterfly diagram and spatial cuts for Run A of Table 2 ($\text{Re}_M \approx 37$) along with its shearless counterpart, where the spatial cuts show the mean fields during the kinematic regime. For $S = 0$ all three fields $\bar{\mathbf{B}}^X$, $\bar{\mathbf{B}}^Y$ and $\bar{\mathbf{B}}^Z$ indeed appear with similar amplitudes and grow at a rate extracted with the test-field method. Their identification as Beltrami fields, however, is all but clear, see Fig. 2, \bar{B}_z^X in lower panel. At least a strong $|\mathbf{k}| = k_1$ harmonic is detectable in each of these fields.

The sheared case is even more obscure. During the kinematic stage there are some indications of a dynamo wave, albeit strongly entangled by fluctuating fields, see Fig. 2, middle panel. More worrying however, the growth rates and amplitudes of the $\bar{\mathbf{B}}^Z$ and $\bar{\mathbf{B}}^X$ fields are very similar and no pronounced features of a Beltrami field can be found in $\bar{\mathbf{B}}^X$. The spatial structure of the $\bar{\mathbf{B}}^Z$ field, expected to be characterized by $k_z = k_1$, is even less clear in this respect than that of the $\bar{\mathbf{B}}^X$ field in the shearless case. However, an identifiable dynamo wave is markedly visible after entering the saturation stage where the growth rate of $\bar{\mathbf{B}}^X$ falls below that of $\bar{\mathbf{B}}^Z$.

For an explanation we refer to the occurrence of a small-scale dynamo at the given values of Re_M and S , checked by integrating Eq. (4) with $\bar{\mathbf{B}} = \mathbf{0}$. It dominates the linear stage and we hypothesize that it “enslaves” the $\bar{\mathbf{B}}^X$ and $\bar{\mathbf{B}}^Z$ fields, and is responsible for the ragged character of their geometries. The fact that with shear there is slower growth than without (see Fig. 2, upper panel), contradictory to the linear analysis, can perhaps be traced down to the reduction of α by the growing magnetic turbulence, cf. the magnetokinetic contribution to α of Rheinhardt & Brandenburg (2010). After the saturation of the small-scale dynamo, the $\alpha^2\Omega$ mode can establish itself on the now settled MHD turbulence, whereas the α^2 mode had perhaps not enough

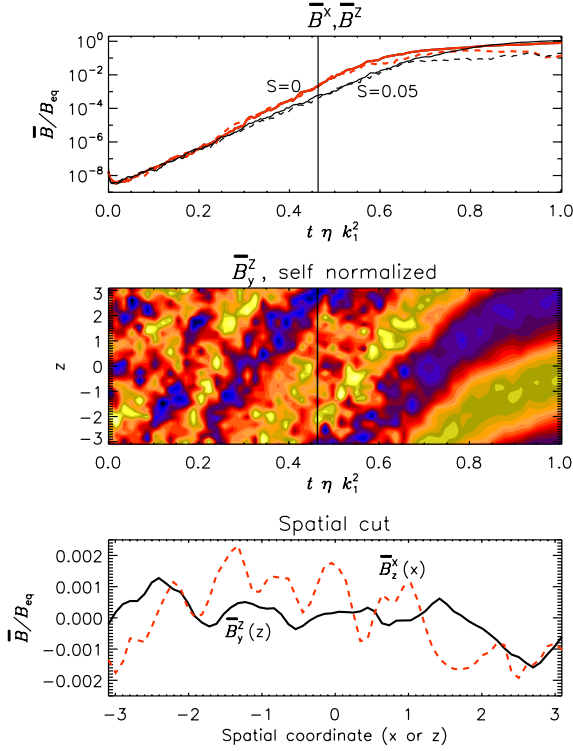


Fig. 2. Time series of the rms values of \overline{B}^Z and \overline{B}^X for Run A and its shearless counterpart. *Top panel:* black/thin for $S = -0.05$; red/thick for $S = 0$; solid for $\overline{B}_{\text{rms}}^Z$, dashed for $\overline{B}_{\text{rms}}^X$. *Middle panel:* butterfly diagram of \overline{B}_y^Z for the sheared case, where \overline{B}_y^Z is normalized to its instantaneous rms value. *Bottom panel:* spatial cut of mean field components at a time during the kinematic regime (indicated by the vertical line in the two other panels); black/solid with shear, red/dashed without.

time to take shape. In the shearless case, in contrast, the small-scale dynamo, if it exists at all, has at least a much smaller growth rate and is hence less capable of influencing the mean field growth. The appearance of a small-scale dynamo in this parameter range is plausible in view of the results in [Schekochihin et al. \(2005\)](#) and [Käpylä et al. \(2008\)](#), although those works use different setups.

5. Deterministic interactions of α^2 and $\alpha^2\Omega$ modes

5.1. Numerical results

Here we report on the results of our simulations, a first set of which is characterized in Table 2. In Fig. 3 we show time series for Run A, which saw a transition from a z varying $\alpha^2\Omega$ dynamo (\overline{B}^Z) to an x varying α^2 dynamo (\overline{B}^X). As is made clear in the bottom panel, there was a prolonged period where the two modes were coexisting while their relative strengths were changing monotonically. However, note that \overline{B}_y^X is stronger than \overline{B}_z^X , that is, the α^2 field is distorted during the transition. Run A was repeated 16 times with the same parameters, but different random seeds, and all these runs exhibited similar behavior. Likewise we performed runs where both the value of η and the numerical resolution (cf. Runs B–D, I, J) were varied. As these additional runs also showed the same transition pattern, we conclude that it is deterministic for this level of shear and forcing. More, we conclude that for these cases the $\alpha^2\Omega$ mode is unstable to the growth of an α^2 mode due to non-linear effects. Runs with the dynamical parameters (S , u_{rms}) of Table 2 inevitably

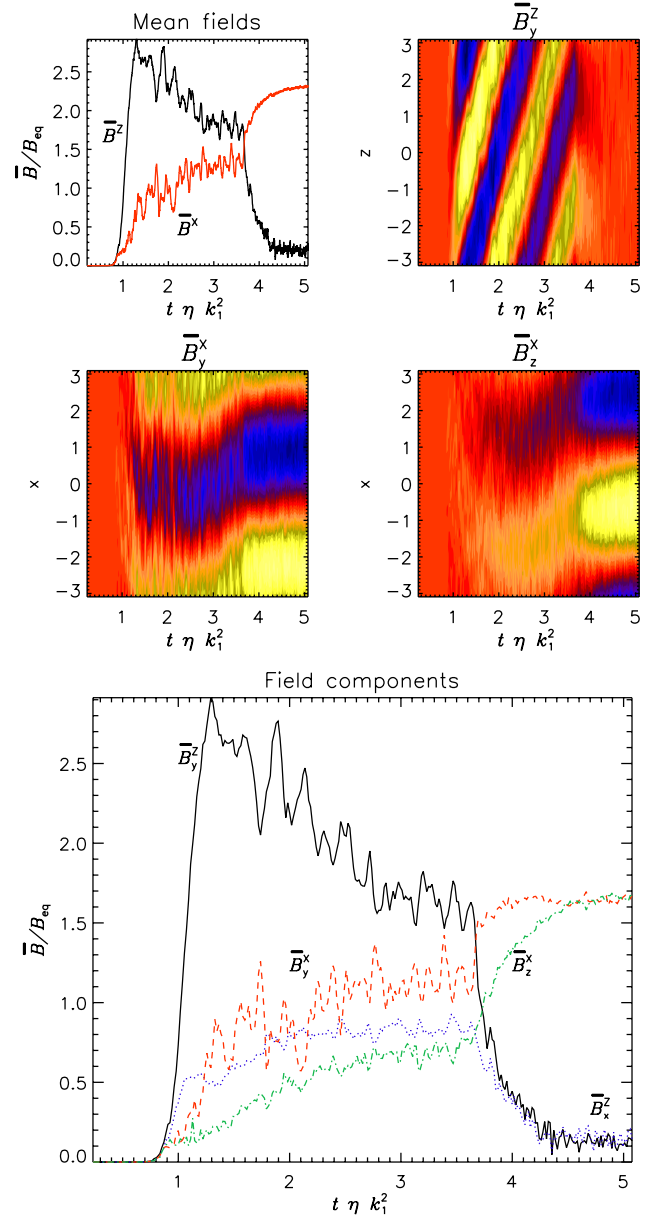


Fig. 3. Time series for Run A. *Upper row:* same quantities as in Fig. 1. *Middle row:* \overline{B}_y^X and \overline{B}_z^X , to be associated with the α^2 mode. Note that the $\alpha^2\Omega$ and α^2 modes coexist during the transition. *Lower panel:* rms values of the components of \overline{B}^X and \overline{B}^Z .

generate α^2 fields from $\alpha^2\Omega$ fields after modest times, runs with significantly different shear will usually (for most of the random seeds) exit the kinematic regime into an $\alpha^2\Omega$ mode, and stay in that mode for a prolonged time with no sign of an α^2 field (but with random transitions into the α^2 mode, see Sect. 6).

Nonetheless all our simulation parameters allow runs to occasionally fail to fully enter the $\alpha^2\Omega$ regime, instead exiting the kinematic regime via a short *transient* $\alpha^2\Omega$ phase into the α^2 mode, as shown in Fig. 4. One might speculate that this “weakness” of the $\alpha^2\Omega$ dynamo is due to strong fluctuations driven by powerful shear (compare the fluctuations of the $\alpha^2\Omega$ and α^2 modes in Fig. 7) but the direct exit into the α^2 mode has also been seen with lower shear as well. We emphasize that this “direct exit” seems to belong neither to the deterministic transitions discussed here nor to the random transitions discussed later.

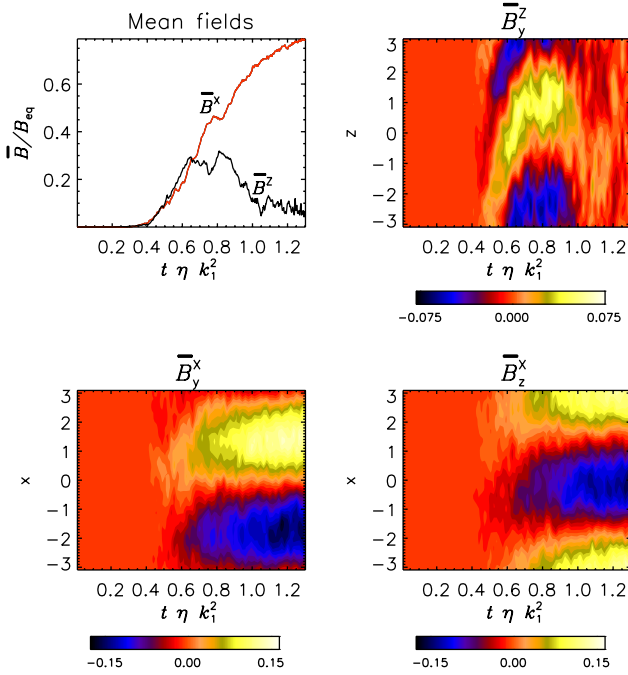


Fig. 4. Time series for a run with same parameters as Run J of Table 2, but different initial conditions, showing a transient, rather than a quasi-stationary $\alpha^2\Omega$ regime. *Top left:* rms values of \overline{B}^Z and \overline{B}^X to be associated with the $\alpha^2\Omega$ (black) and the α^2 mode (red). Note the lack of a well defined phase with a dominating, but declining $\alpha^2\Omega$ mode. *Top right:* butterfly diagram of \overline{B}_y^Z , showing the traveling dynamo wave during the kinematic phase only, but later merely fluctuations. *Bottom:* components of \overline{B}^X .

Table 2. Run parameters of deterministic transitions.

Run	Res.	$-S$	u_{rms}	$-\alpha^\dagger$	η_t^\dagger	Re_M	Pr_M	τ^\ddagger
A	64^3	0.05	0.11	0.04	0.025	37	5	2–3
B	64^3	0.05	0.17	0.04	0.03	26	2.5	2
C	128^3	0.05	0.14	0.04	0.027	44	3	4
D	128^3	0.05	0.14	0.04	0.027	90	6	1.5
I	64^3	0.05	0.15	0.04	0.036	49	1	3
J	64^3	0.05	0.19	0.04	0.035	31	0.5	1.5

Notes. ^(†) Time-averaged values determined through the test-field method using harmonic test fields with $\mathbf{k} = \hat{x}$ or $\mathbf{k} = \hat{z}$. Results are identical due to homogeneity of the time-averaged turbulent velocity. ^(‡) $\tau = t_{\text{dur}}/t_{\text{res}}$ duration of the deterministic transition discussed in Sect. 5. The range for Run A is because of multiple random seeds. In all runs the nondimensional forcing amplitude is $f_0 = 0.04$.

5.2. Analysis: mean-field approach

Clearly, the transition from the $\alpha^2\Omega$ mode to the α^2 one must be a consequence of the back-reaction of $\overline{\mathbf{B}}$ onto the flow. Within the mean-field picture, there are two channels available for it: (i) the back-reaction onto the fluctuating flow, usually described as a dependence of α_{ij} (more seldom η_{ij}) on the mean field and (ii) the back-reaction onto the mean flow by the mean Lorentz force, which might again be decomposed into a part resulting from the fluctuating field, $\overline{\mathbf{j}} \times \overline{\mathbf{b}}$, and one resulting from the mean field, $\overline{\mathbf{J}} \times \overline{\mathbf{B}}$. Here, we will deal with a flow generated by the latter force that straddles the distinction of means and fluctuations: it survives under y -averaging, but vanishes under the xy and yz averaging that reveals the $\alpha^2\Omega$ and α^2 dynamos respectively. For simplicity we consider magnetic field configurations that would

result from a superposition of linear modes of the $\alpha\Omega$ and α^2 dynamos, given in Eqs. (11) and (10) respectively. Such a situation will inevitably occur during the kinematic growth phase if both dynamos are supercritical, but is only relevant for analyzing the back-reaction onto the flow if it at least to some extent continues into the non-linear regime. Our analysis is linear in nature, so while it provides a qualitative framework for understanding the transition process, it is surely not quantitatively accurate.

In order to be able to consider both \overline{B}^X and \overline{B}^Z as mean fields under one and the same averaging, we have now to resort to y averaging. Moreover, for the sake of clarity we will occasionally subject the resulting x and z dependent mean fields further to spectral filtering with respect to these coordinates. That is, we will consider only their first harmonics $\sim e^{ik_1(x+z)}$ as mean fields.

Let us represent the mean field $(\mathbf{B})_y$ as superposition of a \overline{B}^X resembling the (x varying) α^2 mode $\overline{B}^{\alpha\alpha}$ (Eq. (10)) and a \overline{B}^Z resembling the (z varying) $\alpha\Omega$ mode $\overline{B}^{\alpha\Omega}$ (Eq. (11)):

$$\overline{B}^Z = \hat{B}^Z \begin{bmatrix} \sin k_1 z' \\ G \sin(k_1 z' + \phi) \\ 0 \end{bmatrix}, \quad \overline{J}^Z = k_1 \hat{B}^Z \begin{bmatrix} -G \cos(k_1 z' + \phi) \\ \cos k_1 z' \\ 0 \end{bmatrix},$$

$$\overline{B}^X = \hat{B}^X \begin{bmatrix} 0 \\ H \sin k_1 x \\ \cos k_1 x \end{bmatrix}, \quad \overline{J}^X = k_1 \hat{B}^X \begin{bmatrix} 0 \\ \sin k_1 x \\ H \cos k_1 x \end{bmatrix}, \quad (20)$$

with $z' \equiv z - ct$, recalling that c is the speed of the dynamo wave (Eq. (12)). In the above, $\pi/4 \leq \phi \leq 3\pi/4$ and $G, H, k_1 > 0$ are appropriate for $\alpha > 0$. The parameters G and H capture the difference in the strengths of the y and z components of $\overline{\mathbf{B}}^{\alpha\alpha}$ or the x or y components of $\overline{\mathbf{B}}^{\alpha\Omega}$, respectively. We expect $G > 1$ as shear amplifies the y component of an $\alpha^2\Omega$ mode well above its x component. The inclusion of the parameter H , which is unity for pure α^2 modes will be justified below, see the different strengths of \overline{B}_y^X and \overline{B}_z^X in Fig. 3, lower panel.

The mean Lorentz force $\overline{\mathbf{F}}_L = \overline{\mathbf{J}} \times \overline{\mathbf{B}}$ for the superimposed fields can be written as

$$\overline{\mathbf{F}}_L = \langle \mathbf{F}_L \rangle_y$$

$$= k_1 \hat{B}^X \hat{B}^Z \cos k_1 x [G \cos(k_1 z' + \phi) + H \sin k_1 z'] \hat{y} + \nabla\Phi. \quad (21)$$

As the Mach numbers were found to be small throughout, we assume incompressibility and hence drop the potential component $\nabla\Phi$. Further, we assume that $\overline{\mathbf{F}}_L$ and the mean velocity driven by it are simply linked by a coefficient $K \approx 1/\nu_T k_1^2$, where the total viscosity ν_T is the sum of the molecular ν , and the turbulent viscosity ν_t . Thus we can approximate the mean velocity due to the interaction of the superimposed mean fields as

$$\overline{U}_L = U_L \cos k_1 x [G \cos(k_1 z' + \phi) + H \sin k_1 z'] \hat{y}, \quad (22)$$

where $U_L = K k_1 \hat{B}^X \hat{B}^Z$. Clearly, this flow, having merely a y component, shows quadrupolar geometry in the $x-z$ plane as $\overline{U}_{L,y}$ can be rewritten in the form $U'_L \cos k_1 x \cos(k_1 z' + \phi')$ with a new amplitude and phase, U'_L and ϕ' .

The simulations show indeed a dominant part of that shape in the Lorentz-force generated mean flow as can be seen from Fig. 5. There the y averaged U_y is shown together with its Fourier constituent $\sim e^{ik_1(x+z)}$. The latter contains approximately 10% of the energy in this component, or $U'_L = \overline{U}_{y,\text{rms}}/3$, indicating that the assumptions made in deriving (22) are reasonably well justified in a non-linear system.

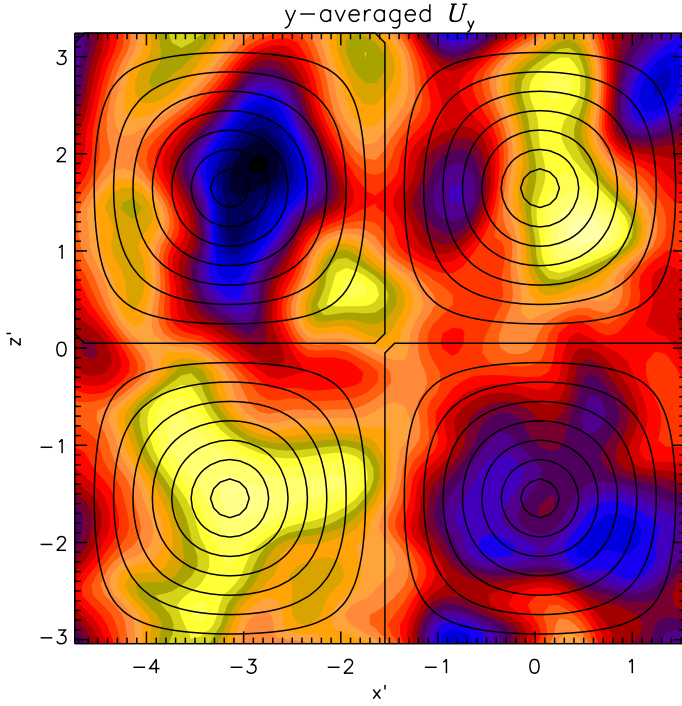


Fig. 5. $\langle U_y \rangle_y$ for Run A, taken at early time ($t = 1.45 t_{\text{res}}$) when $\bar{\mathbf{B}}^X$ is still of only modest strength. Plotting area is shifted in x and z to make the quadrupolar geometry clear. Overplotted contours: quadrupolar constituent $\sim \cos k_1 x' \cos k_1 z'$.

Upon interaction with a $\bar{\mathbf{B}}^X$ or a $\bar{\mathbf{B}}^Z$ of the form (20), the mean flow $\bar{\mathbf{U}}_L$ in (22) generates an $\bar{\mathcal{E}}_x(z)$ and $\bar{\mathcal{E}}_z(x)$, respectively.

5.2.1. Dominating $\alpha^2\Omega$ mode

If $\hat{B}^Z \gg \hat{B}^X$, then $\bar{\mathbf{B}}^X$ can be treated as a perturbation, and we can drop higher order terms in \hat{B}^X . Accordingly, the z -averaged EMF due to the flow $\bar{\mathbf{U}}_L$ is

$$\bar{\mathcal{E}}^X = \langle \bar{\mathbf{U}}_L \times \bar{\mathbf{B}}^Z \rangle_z = \frac{Kk_1}{2} \hat{B}^X \hat{B}^{Z^2} (G \sin \phi - H) \cos k_1 x \hat{z}. \quad (23)$$

The curl of this EMF is

$$\nabla \times \bar{\mathcal{E}}^X = \hat{B}^X I \sin k_1 x \hat{y}, \quad I \equiv \frac{Kk_1^2 \hat{B}^{Z^2}}{2} (G \sin \phi - H). \quad (24)$$

If $G \sin \phi > H$, then $I > 0$ and for $H > 0$ this EMF reinforces $\bar{\mathbf{B}}^X = \hat{B}^X H \sin k_1 x$. Thus we see that the inclusion of the parameter H in the ansatz for $\bar{\mathbf{B}}^X$, Eq. (20), was justified as $\bar{\mathbf{B}}^X$ receives enhanced forcing in comparison to $\bar{\mathbf{B}}^Z$.

5.2.2. Dominating α^2 mode

If $\hat{B}^X \gg \hat{B}^Z$ then we can in turn treat $\bar{\mathbf{B}}^Z$ as a perturbation. Further, as the system is dominated by the α^2 mode, we will have $H \sim 1$. In this case we find

$$\begin{aligned} \bar{\mathcal{E}}^Z &= \langle \bar{\mathbf{U}}_L \times \bar{\mathbf{B}}^X \rangle_x \\ &= \frac{Kk_1}{2} \hat{B}^Z \hat{B}^{X^2} [G \cos(k_1 z' + \phi) + H \sin k_1 z'] \hat{x}, \end{aligned} \quad (25)$$

and

$$\nabla \times \bar{\mathcal{E}}^Z = \hat{B}^Z \frac{Kk_1^2}{2} \hat{B}^{X^2} [H \cos k_1 z' - G \sin(k_1 z' + \phi)] \hat{y}. \quad (26)$$

We can write

$$H \cos k_1 z' - G \sin(k_1 z' + \phi) = [(H \sin \phi - G) \sin(k_1 z' + \phi)]_1 + [H \cos \phi \cos(k_1 z' + \phi)]_2. \quad (27)$$

If $H \sin \phi - G < 0$, as expected since $H \approx 1$, $G > 1$, term [1] in (27) will act to damp $\bar{\mathbf{B}}^Z$, that is, the perturbative $\alpha^2\Omega$ wave. Further, term [2] is opposite in sign to the time-derivative of such a wave, so it slows or reverses the direction of wave-propagation.

5.2.3. Mean-field evolution

Here we assume again domination of the $\alpha^2\Omega$ mode, that is, $\hat{B}^Z \gg \hat{B}^X$. With Eqs. (7) and (24) the eigenvalue problem for the modified α^2 field $\bar{\mathbf{B}}^X$ is then (adopting $k_x = k_1$, $k_z = 0$)

$$\lambda^X \bar{\mathbf{B}}^X = \begin{bmatrix} -\eta_T k_1^2 & 0 & 0 \\ S & -\eta_T k_1^2 & -i(\alpha k_1 + I) \\ 0 & i\alpha k_1 & -\eta_T k_1^2 \end{bmatrix} \bar{\mathbf{B}}^X, \quad (28)$$

with eigenvalues

$$\lambda_{\pm}^X = -\eta_T k_1^2 \pm \sqrt{\alpha k_1 (\alpha k_1 + I)}. \quad (29)$$

Making the approximation $I \gg \alpha k_1$, similar to the $\alpha\Omega$ approximation $S \gg \alpha k_1$, we find

$$\lambda_{\pm}^X = -\eta_T k_1^2 \pm \sqrt{\alpha I k_1}. \quad (30)$$

The above should be compared with the growth rate of the $\alpha\Omega$ dynamo, $\lambda^{\alpha\Omega}$ from (13) which is not touched by the occurrence of I . The $\alpha\Omega$ dynamo saturates when α has been quenched such that the product αS settles at the marginal value $|\alpha S| = 2\eta_T^2 |k_1|^3$. If the parameter I becomes comparable with the shear, i.e., $I \sim S$, then $\bar{\mathbf{B}}^X$ might grow even when the $\alpha^2\Omega$ field is saturated, i.e. $\lambda_{\pm}^X \gg \Re(\lambda^{\alpha\Omega}) = 0$. In other terms, the saturated $\alpha^2\Omega$ mode is unstable to the growth of a *fratricidal* α^2 field, so the transition will take a well defined time from the onset of the non-linear stage, determined by λ^X .

We test this theory for Run A at the time of Fig. 5, $t = 1.45 t_{\text{res}}$, extracting G and H from the relative strengths of the x and y or y and z components of the mean fields $\bar{\mathbf{B}}^Z$ or $\bar{\mathbf{B}}^X$, respectively, after a projection onto the first harmonics; see Eq. (20). The parameter I is calculated from the magnetic and velocity fields using

$$I = \frac{k_1 \hat{B}^Z U_L}{2 \hat{B}^X} (G \sin \phi - H), \quad (31)$$

with $U_L = U'_L / \sqrt{G^2 + H^2 - 2GH \sin \phi}$, where U'_L is the amplitude of the quadrupolar constituent of the velocity field seen in Fig. 5. We find $U'_L \simeq 0.07$, $H \simeq 2.9$, $G \simeq 4.9$, $I \simeq 0.09$, and confirm that $\phi \simeq \pi/4$. As $I > S = 0.05$, the growth of the x varying mode even when the $\alpha^2\Omega$ mode is saturated is not surprising. Repeating this run 16 times with different random seeds (keeping the control parameters fixed) changed the occurrence time of the transition by only one resistive time, suggesting that the transition is an essentially deterministic process.

We have never seen a reverse transition from the α^2 state back to the $\alpha^2\Omega$ state. This may be understood in terms of interacting modes, with the $\alpha^2\Omega$ mode being suppressed once the α^2 mode is dominating; see Sect. 5.2.2.

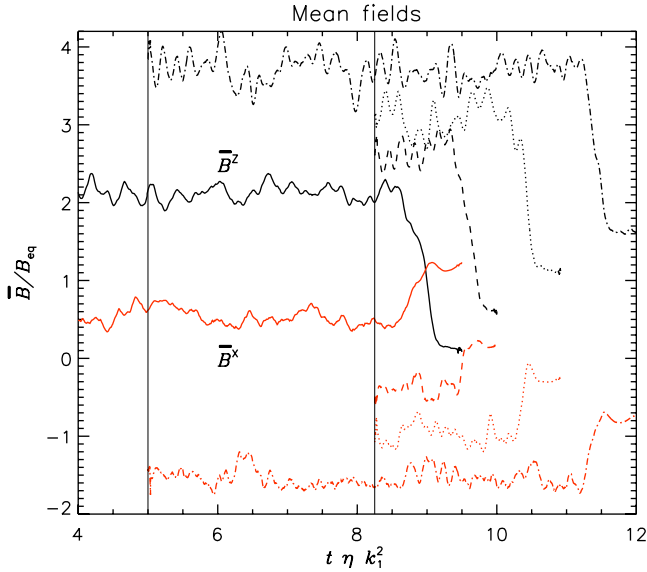


Fig. 6. Time series for Run F (solid lines), with rms values of \bar{B}^Z (black) and \bar{B}^X (red). Broken lines: restarts from the main run with new random seeds, vertically offset for visibility. All the runs end up with the same energies in \bar{B}^X and \bar{B}^Z . Vertical lines: restart times.

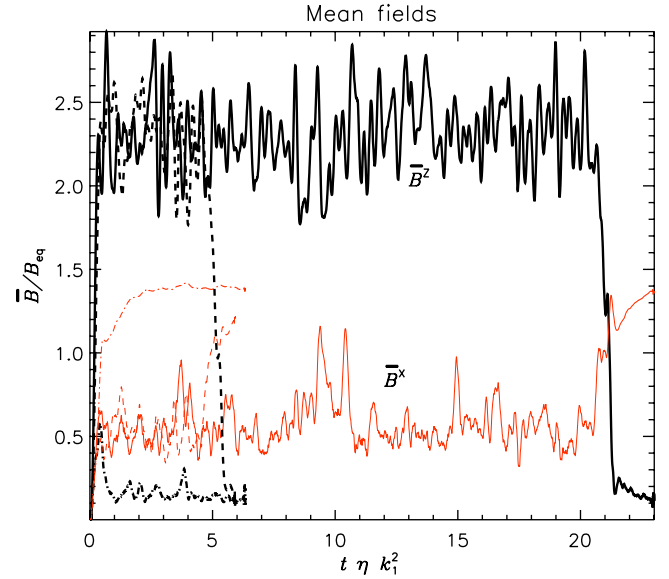


Fig. 7. Time series of Run G (solid, thick) along with a sibling run (dashed) with different seeds, showing significant differences in the transition start time. Dash-dotted: a run which never entered the $\alpha^2\Omega$ regime. Colors as in Fig. 6.

Table 3. Run parameters for random transitions.

Run	f_0	$-S$	u_{rms}	$-\alpha^\dagger$	η_l^\dagger	Re_M	Pr_M	τ^\dagger
0	0.04	0.1	0.11	0.035	0.035	6.8	1	135
H	0.03	0.1	0.085	0.017	0.037	27	5	25
K	0.04	0.1	0.11	0.017	0.012	60	10	18, 36 [‡]
L	0.05	0.1	0.14	0.015	0.005	90	10	22
M	0.04	0.2	0.11	0.013	0.012	30	5	8
G	0.03	0.2	0.099	0.01	0.16	63	10	5, 20 [‡]
E	0.05	0.2	0.13	0.04	0.023	90	10	N/A
F	0.05	0.2	0.14	0.02	0.1	90	10	5, 9 [‡]
N	0.05	0.3	0.14	0.03	0.012	90	10	3

Notes. ([†]) See Table 2. ([‡]) $\tau = t_{trans}/t_{res}$ is the time when the transition occurred; for F, G and K from multiple realizations with differing random seeds; see Fig. 8. Run E is highlighted as it does not exhibit a stationary $\alpha^2\Omega$ state. Resolution 64^3 in all runs.

6. Random transitions

6.1. Non-interacting modes

Not all transitions fit into the above deterministic picture of interacting $\alpha^2\Omega$ and α^2 modes. The behavior above and below the shear value $S = -0.05$ that applies to the runs in the previous section is qualitatively different. In Fig. 6 we present a set of time series of the rms values of \bar{B}^Z and \bar{B}^X , all related to Run F of Table 3. Secondary runs were performed by branching off from the original simulation either at $t = 5t_{res}$, when the $\alpha^2\Omega$ mode is well established and stationary, or at $t = 8.25t_{res}$, immediately before the transition to the α^2 mode in the primary run is launched. The only difference between all these runs is in the random seed, which is used by the forcing algorithm. In all, the time until the transition starts varies by $\approx 2.5t_{res}$, and many more turbulent turnover times ($Re_M k_1^2/k_1^2 \approx 800$ turbulent turnover times per resistive time). The time elapsed during a transition is always of the order of $t_{res}/2$, unlike $3t_{res}$ for the process seen in Fig. 3. Thus it is suggestive to assume that there might be a very slow, still essentially deterministic process, preparing the

transition, which is likely resistive in nature as that is the longest obvious “native” timescale of the system. Slow resistive effects are known to exist in dynamos, for example the slow resistive growth of α^2 dynamos in periodic systems. However, transitions can indeed occur at very different times including the extreme case in which a run never develops a quasi-stationary $\alpha^2\Omega$ mode, but instead enters the α^2 state almost immediately after the end of the kinematic phase, see Fig. 7 (run G of Table 3). We believe therefore that under certain circumstances the transition process is not a deterministic one, in that it is impossible to predict or at least estimate the time until the transition. Figure 8 is a synopsis of simulations that belong to that type, hence do not show the instability discussed in Sect. 5. Note that, while corresponding setups without shear are known to enable α^2 modes for the entire Re_M range studied (Brandenburg 2009), we cannot rule out that the α^2 mode is sub-critical for $Re_M = 10, S = -0.1$ (i.e., it is possible that the run denoted by the bottom left diamond in the upper panel did not transition because it simply could not).

The picture of random transitions is different from the interacting mode one of Sect. 5 in several interesting ways. Crucially, the $\alpha^2\Omega$ mode is here at least meta-stable against growth of the α^2 mode, as evinced by its prolonged life-time (hundreds of turbulent times) and the small magnitude of \bar{B}^X , which further is not dominated by an α^2 mode. A reasonable working hypothesis for the cases of Sect. 5 is then that, there, the α^2 mode is the only stable solution and, as soon as the nonlinear stage has been entered, it starts to devour the $\alpha^2\Omega$ one, settling after a time which is related to basic parameters of the system and hence not random. In contrast, for the cases considered here, we conclude that both the α^2 and the $\alpha^2\Omega$ solutions are indeed stable (not only metastable) and the latter has a well extended basin of entrainment. Due to its higher growth rate the system settles first in the $\alpha^2\Omega$ mode and suppresses the α^2 mode efficiently. A transition to the latter can only occur if a random fluctuation in the forcing is strong enough to push the system over the separatrix into the basin of entrainment of the α^2 mode. This may happen after only a long time or even never during a simulation’s run time, cf. diamond and square symbols, respectively, in Fig. 8,

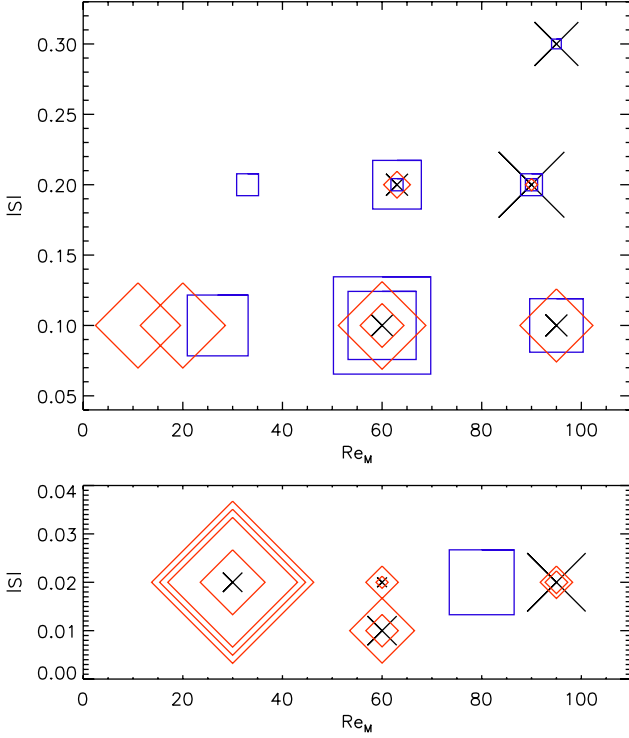


Fig. 8. Synopsis of runs which did not exhibit the instability discussed in Sect. 5. Crosses/black: a significant $\alpha^2\Omega$ mode was never developed (cf. Fig. 4), symbol size indicates the corresponding number of runs (1, 2 or 3). Square/blue: a transition occurred, size represents the time until transition (4 to $25t_{\text{res}}$). Diamond/red: the $\alpha^2\Omega$ stage was entered, but no transition occurred. Size represents the time span of simulation (5 to $35t_{\text{res}}$). Runs at the same position differ only in random seeds. *Upper panel:* high-shear runs, see Table 3 for those exhibiting a random transition. *Lower panel:* low-shear runs. Symbols scaled down by a factor of 3 with respect to upper panel. All runs in the lower panel had $f_0 = 0.04$.

see also the absence of a transition in Fig. 1 where $S = -0.1$, $\text{Re}_M = 20$. From these data one can also derive that the tendency to leave the $\alpha^2\Omega$ state by a random transition increases both with growing shear and Re_M (note the corresponding reduction in the blue squares’ size = time until transition in Fig. 8). Although one would expect the basin of entrainment of the $\alpha^2\Omega$ mode to enlarge with growing S , it is conceivable that at the same time the level of velocity fluctuations is raised, making transitions eventually more likely. Growing Re_M can readily be thought of increasing the fluctuation level and hence the transition probability likewise. As already mentioned in Sect. 5, we see in addition “direct exits” from the kinematic stage into a saturated α^2 dynamo; see Fig. 8 (cross symbols) and Fig. 9.

Given that the examples for the first scenario (Table 2) differ from those for the second (Table 3) mainly in their lower rate of shear, our conclusion seems reasonable as stronger shear should result in a clearer preference of the $\alpha^2\Omega$ mode because the α^2 mode does not feel the shear. Or, in other terms, from a certain shear rate S on, the $\alpha^2\Omega$ mode should acquire a basin of entrainment with a finite “volume” that grows with S . If this picture is true, transitions in the two scenarios should have clearly different characteristics, and indeed, the transition in Fig. 6 is markedly faster than that seen in Fig. 3.

Once the shear rate is dropped markedly below $S = 0.05$, the typical value for *deterministic* transitions, the system again seems to settle in a domain similar to the high-shear ($S \geq 0.1$) one, namely one with both the α^2 and the $\alpha^2\Omega$ modes being

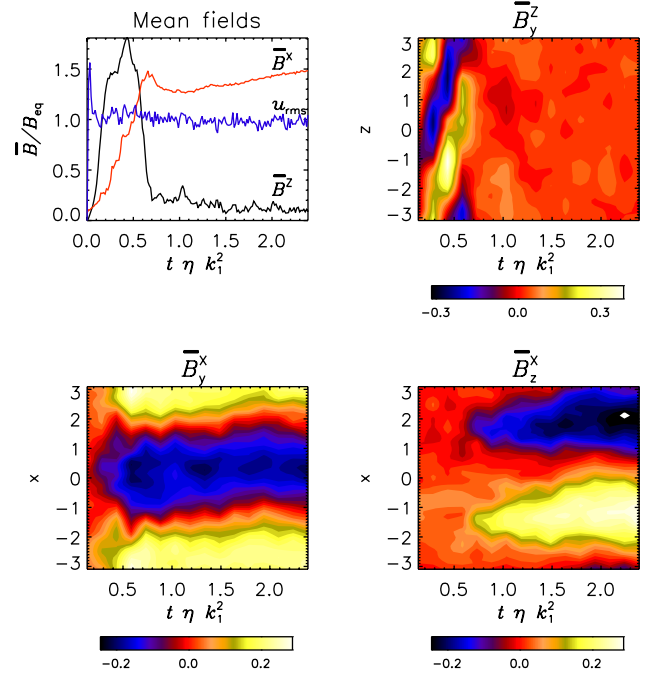


Fig. 9. Time series for Run E of Table 3 showing a transient, not a stationary $\alpha^2\Omega$ regime. For explanations see Fig. 4. Note the considerably faster growth of the $\alpha^2\Omega$ mode during the kinematic phase and the lack of a well defined phase with a dominating, but declining $\alpha^2\Omega$ mode.

stable. However, entering into the α^2 state immediately after the kinematic stage (the “direct exit”) appears now to be more likely, while at the same time random transitions away from a *settled* $\alpha^2\Omega$ state become extremely rare: Over a run time of $3 \times 10^3 t_{\text{res}}$ accumulated over several runs with $S = 0.01, 0.02$ as well as target values of Re_M around 30, 60, and 90, only one transition was observed (for $\text{Re}_M = 80$, $\text{Pr}_M = 5$, $S = 0.02$, after $8 \times 10^2 t_{\text{res}}$); see also Fig. 8, lower panel. Plausibility arguments for the occurrence of this “low shear” domain, in particular for the apparent regaining of a finite basin of entrainment by the $\alpha^2\Omega$ mode which has to be implied, are not in sight.

As in the transitions discussed in Sect. 5, we have not here seen the α^2 mode transition back into the $\alpha^2\Omega$ mode. Some attempts were made to provoke this reverse transition by perturbing the α^2 state with a (sufficiently strong) $\alpha^2\Omega$ mode. While in some runs it indeed took over, velocities were attained for which the numerics are unreliable, and often proved numerically unstable, making the results inconclusive. However, such a behavior is not entirely surprising as the $\alpha^2\Omega$ saturation process can anyway be somewhat wild, cf. Fig. 4.

The absence of *spontaneous* reverse transitions appears plausible insofar the time variability of the α^2 mode is much smaller than that of the $\alpha^2\Omega$ mode, which can clearly be seen in Fig. 10 for Run H. That is, events capable of pushing the system over the separatrix are simply much rarer. Significantly longer integration times are likely needed for their eventual detection, but it is also conceivable that the triggering event never shows up.

6.2. Large scale patterns

Run H will be examined here in more detail. Curiously, $\langle U_y \rangle_y$ taken just during the transition as shown in Fig. 11 does not show the quadrupolar pattern of Fig. 5. It is therefore not surprising that the butterfly diagrams in Fig. 12 do not show a direct transition from the $\alpha^2\Omega$ to the α^2 dynamo, as \overline{B}_z^x develops significantly

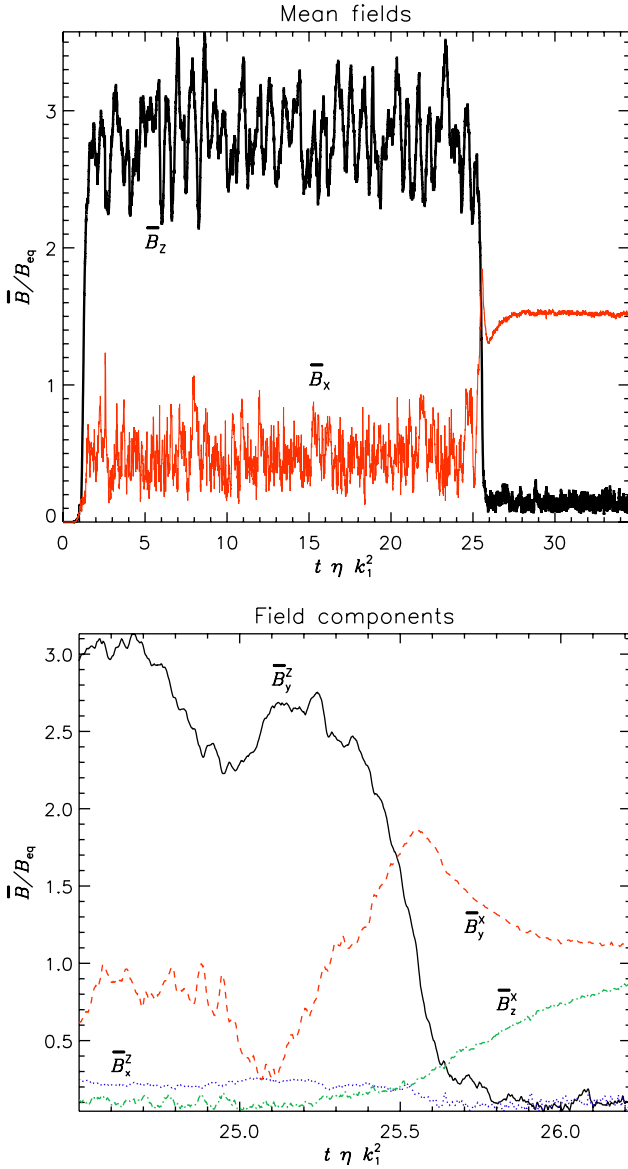


Fig. 10. Time series of Run H. *Upper panel:* rms values of \bar{B}^X and \bar{B}^Z . Note the long time before the transition starts in comparison to Run F (see Fig. 6) and the dramatic difference in the fluctuation levels before and after the transition. *Lower panel:* rms values of the components. Note the strong difference between \bar{B}_y^Z and \bar{B}_x^Z , expected for an $\alpha^2\Omega$ field. More significantly, notice that \bar{B}_y^X develops before \bar{B}_z^X .

later than \bar{B}_y^X . This is clearly visible in Fig. 10, lower panel. As consideration of the mean flow due to the Lorentz force of the mean field alone is obviously not fruitful in explaining this transition, we recall that the back-reaction of the mean field onto the turbulence opens another channel of nonlinear interaction.

According to elementary mean-field dynamo theory, the α effect is caused by the helicity in the flow: $\alpha \sim \langle \mathbf{w} \cdot \mathbf{u} \rangle$, where $\mathbf{w} \equiv \nabla \times \mathbf{u}$ is the fluctuating vorticity. Further, the back-reaction of the mean field on the turbulence, which saturates the dynamo, is assumed to be captured by the current helicity $\langle \mathbf{j} \cdot \mathbf{b} \rangle$. It is often related to the magnetic helicity $\langle \mathbf{a} \cdot \mathbf{b} \rangle$ and thought to reduce the original α by producing a *magnetic* contribution of opposite sign. In Fig. 13 we present time-series of the power spectra of these helicity correlators across the transition. However, we see no clear signal around the transition event.

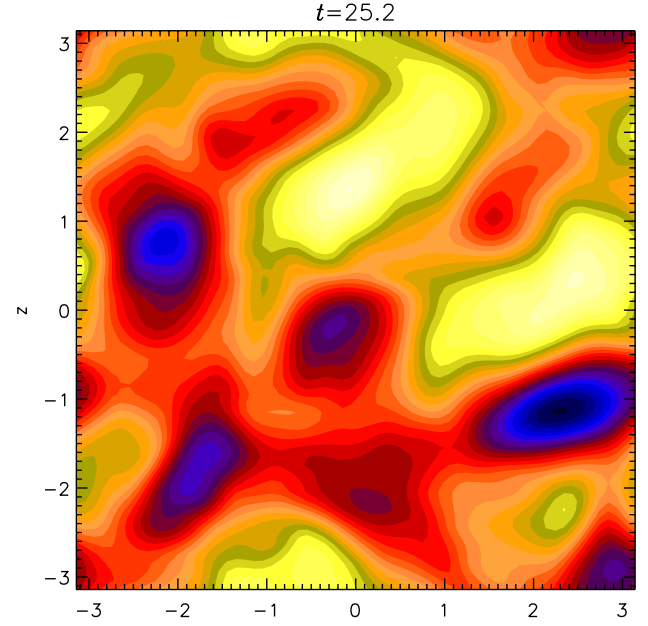


Fig. 11. $\langle U_y \rangle$ taken during the transition of Run H shown in Fig. 10 ($t = 25.2t_{\text{res}}$). Note the lack of a quadrupolar geometry.

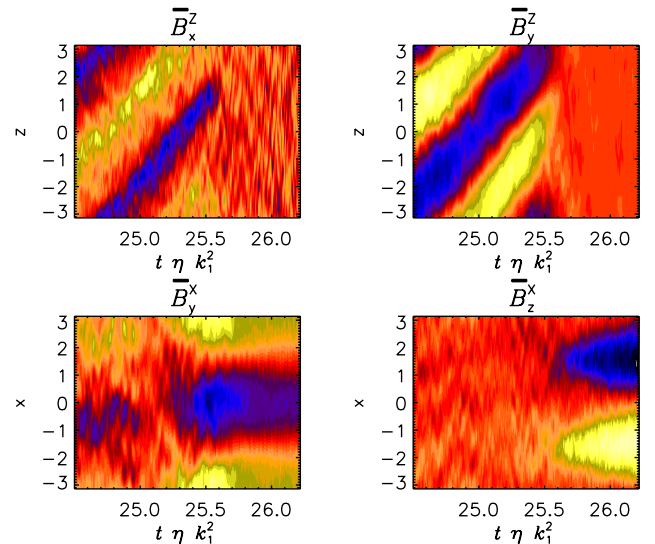


Fig. 12. Butterfly diagrams for Run H (see Fig. 10). Note that \bar{B}_y^X develops before \bar{B}_z^X , i.e., \bar{B} does not transition from an $\alpha^2\Omega$ field straight to an α^2 one.

6.3. Mean-field analysis with y averaging

To examine the problem more closely, we recall Eq. (18) for a mean defined by the y average:

$$\bar{\mathcal{E}}_i(x, z) = \alpha_{ij}(x, z) \bar{B}_j(x, z) + \eta_{ijk}(x, z) \bar{B}_{j,k}(x, z). \quad (32)$$

It is clear that the Fourier constituents of α_{ij} and η_{ijk} with wavenumber k_1 in both x and z (the quadrupolar constituents) can create an EMF $\bar{\mathcal{E}}^X$ out of a field \bar{B}^Z , both with the same wavenumber:

$$\bar{\mathcal{E}}_i^X = \left\langle \alpha_{i1}^{11} \bar{B}_x^Z + \alpha_{i2}^{11} \bar{B}_y^Z + \eta_{i13}^{11} \frac{\partial \bar{B}_x^Z}{\partial z} + \eta_{i23}^{11} \frac{\partial \bar{B}_y^Z}{\partial z} \right\rangle, \quad (33)$$

where the superscripts indicate the coefficients to be the Fourier constituents $\sim e^{ik_1(x+y)}$ and \bar{B}_z^Z is assumed to vanish. Note that

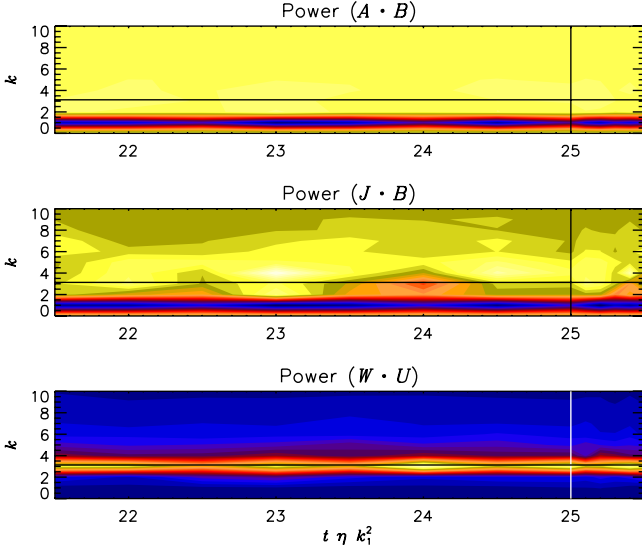


Fig. 13. Time series of the helicity power spectra for Run H. Horizontal line: forcing wavenumber $k_f \approx 3.1$. Vertical line: border between low-resolution observations (every $0.5t_{\text{res}}$) for $t < 25t_{\text{res}}$ and higher-resolution observations (every $0.1t_{\text{res}}$) for $t > 25t_{\text{res}}$. Possible features in the latter range are likely due to the increased temporal resolution.

each of them is actually given by four values, e.g., the two amplitudes and phases in:

$$\alpha_{ij}^{11} = \alpha_{ij}^c \cos(k_1 x + \phi_{ij}^c) \cos k_1 z + \alpha_{ij}^s \cos(k_1 x + \phi_{ij}^s) \sin k_1 z. \quad (34)$$

The coefficients relevant for the generation of \bar{B}_y^X (from \bar{E}_z^X alone) are α_{31}^{11} , α_{32}^{11} , η_{313}^{11} and η_{323}^{11} . We have used the test-field method (see Sect. 3.2) to find them and present the results in Fig. 14. They turn out to be surprisingly large, when compared to the rms velocity (e.g., $(\alpha_{31}^{c2} + \alpha_{31}^{s2})^{1/2} \gtrsim 4u_{\text{rms}}$) and some may show a trend across the transition from the $\alpha^2\Omega$ to the α^2 field. This overall trend is hypothesized to be due to the increase in u_{rms} that accompanies the transition from a stronger $\alpha^2\Omega$ field to a weaker α^2 field with less potential to inhibit the flow. It is interesting that the large transport coefficients (ignoring α_{33}^{11} and η_{311}^{11} which are without effect) are all those which generate an \bar{E} out of \bar{B}_z^Z , i.e., out of the component that feels the effect of shear. We speculate that these coefficients feel the shear quite strongly.

7. Discussion and conclusions

We have demonstrated that, while $\alpha^2\Omega$ modes are kinematically preferred to α^2 modes in homogeneous systems that support both, the α^2 mode acts in a fratricidal manner against the former after the nonlinear stage has been reached. This transition can occur in at least two different fashions. Further, we have not observed the reverse process. One of the two transition processes, based on superposed $\alpha^2\Omega$ and α^2 modes, operates in a basically deterministic fashion through a large-scale velocity pattern generated by the interaction of the modes. In contrast, we interpret the mechanism of the second process, which may start only many resistive times past the saturation of the $\alpha^2\Omega$ dynamo, by assuming that both the $\alpha^2\Omega$ and the α^2 modes are stable solutions of the nonlinear system. Transitions occur if due to the random forcing a sufficiently strong perturbation builds up which tosses the system out of the basin of entrainment of the $\alpha^2\Omega$ mode into that of the α^2 mode. This hypothesis is bolstered by both the random timing of these transitions and by the large time-variability

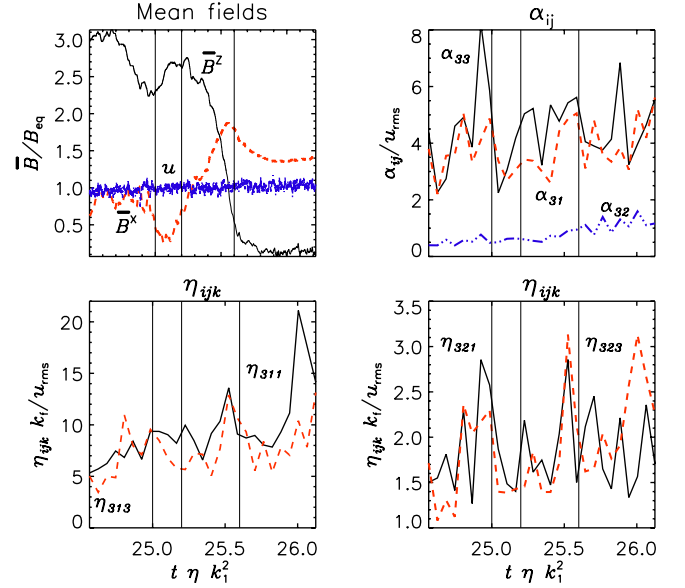


Fig. 14. Run H. *Upper left panel:* rms values of \bar{B}^x , \bar{B}^z and u ($u_{\text{rms}} = \langle u^2 \rangle^{1/2}$), cf. Fig. 10. Remaining panels: selected quadrupolar moments of α_{ij} and η_{ijk} determined by the test-field method and given by $(\alpha_{ij}^{c2} + \alpha_{ij}^{s2})^{1/2}$, see Eq. (34); likewise for η_{ijk} . Normalization is by the temporally averaged u_{rms} , as u_{rms} undergoes a slow, steady drift over time. Vertical lines mark the times of events visible in the first panel.

seen in the amplitude of the $\alpha^2\Omega$ field. A return seems to be much less likely as the level of fluctuations of the α^2 mode is, by contrast, greatly reduced. Random transitions are influenced by the shear rate. Above the shear level of $S = 0.05$ associated with deterministic transitions, eventual random transitions appear to be inevitable. Markedly below that level they are, at best, extremely rare. This suggests strongly that the vulnerability of an $\alpha^2\Omega$ mode to transitions increases with its dynamo number.

These results fit with earlier work studying dynamos whose non-linear behavior is fundamentally different from their linear one (e.g., Fuchs et al. 1999). While our simulations are limited to Cartesian, cubic, shearing-periodic domains, they are particularly exciting given that the only dynamo which has been observed over a long baseline and which could be either $\alpha^2\Omega$ or α^2 , the solar dynamo, indeed shows differing modes of operation (regular cycles vs. deep minima). The results are also disturbing in that we have evidence for non-deterministic, rare (as they occur on scales of multiple resistive times or hundreds of turbulent turnovers) mode changes that show no evidence for a return. While a bifurcation between different stable modes has long been an acknowledged possibility for dynamos (Brandenburg et al. 1989; Jennings 1991; Covas & Tavakol 1997), a rare, stochastic, possibly uni-directional transition is perhaps the most troublesome consequence of such bifurcations except for the ultimate self-extinction.

Given that the mean-field transport coefficients have been systematically derived for many of the runs, it may sound plausible to study the nonlinear stability of different dynamo regimes by means of mean field models. This would allow to construct a stability map for the system to test the hypothesis made in the paper. However, there are two difficulties: firstly, the derived transport coefficients apply only for the specific mean field for which they have been calculated, i.e. they are not the functional derivatives of the mean EMF with respect to the mean field or current density and to our knowledge the technology to do better does not yet exist. This deficiency applies only to the non-linear regime, of course. Secondly, to overcome this restriction one

could assume that the transport coefficients are smooth functionals of the mean field and so can be obtained from a finite set of data points by interpolation. This would require only to perturb the system into neighboring states, from which, however, it would tend to return to the original state in a self-regulated way. As the transport coefficients can only be calculated for sufficiently slowly changing flows, the set of obtainable data points would be strongly limited.

The $\alpha\Omega$ dynamo is believed to be common and important for systems like the Sun or accretion disks, which all have long lifetimes compared to turbulent turnover times. It is then a daunting possibility that we could be forced to stretch our simulations over very long temporal base-lines to find the actual long-lasting field configuration. More positively, our result, while in a different geometry, increases the importance of recent work on non-oscillatory $\alpha\Omega$ and oscillatory α^2 modes in spherical shells for the solar dynamo (Mitra et al. 2010; Schrunner et al. 2011).

Acknowledgements. We thank the anonymous referee for having made detailed suggestions that have helped improving the clarity of the paper. We acknowledge the allocation of computing resources provided by the Swedish National Allocations Committee at the Center for Parallel Computers at the Royal Institute of Technology in Stockholm and the National Supercomputer Centers in Linköping. This work was supported in part by the European Research Council under the AstroDyn Research Project No. 227952 and the Swedish Research Council Grant No. 621-2007-4064.

References

- Baryshnikova, I., & Shukurov, A. 1987, *Astron. Nachr.*, 308, 89
 Brandenburg, A. 2001, *ApJ*, 550, 824
 Brandenburg, A. 2009, *ApJ*, 697, 1206
 Brandenburg, A., & Subramanian, K. 2005, *Phys. Rep.*, 417, 1
 Brandenburg, A., Krause, F., Meinel, R., Moss, D., & Tuominen, I. 1989, *A&A*, 213, 411
 Brandenburg, A., Rädler, K.-H., & Schrunner, M. 2008a, *A&A*, 482, 739
 Brandenburg, A., Rädler, K.-H., Rheinhardt, M., & Käpylä, P. J. 2008b, *ApJ*, 676, 740
 Charbonneau, P. 2010, *Liv. Rev. Sol. Phys.*, 7, 3
 Covas, E., Ashwin, P., & Tavakol, R. 1997, *Phys. Rev. E*, 56, 6451
 Christensen, U., Olson, P., & Glatzmaier, G. A. 1999, *Geophys. J. Int.*, 138, 393
 Covas, E., & Tavakol, R. 1997, *Phys. Rev. E*, 55, 6641
 Eddy, J. A. 1976, *Science*, 286, 1198
 Fuchs, H., Rädler, K.-H., & Rheinhardt, M. 1999, *Astron. Nachr.*, 320, 129
 Grote, E., & Busse, F. 2000, *Phys. Rev. E*, 62, 4457
 Haugen, N. E. L., Brandenburg, A., & Dobler, W. 2004, *Phys. Rev. E*, 70, 016308
 Hubbard, A., & Brandenburg, A. 2009, *ApJ*, 706, 712
 Hubbard, A., Del Sordo, F., Käpylä, P. J., & Brandenburg, A. 2009, *MNRAS*, 398, 1891
 Jennings, R. L. 1991, *Geophys. Astrophys. Fluid Dyn.*, 57, 147
 Käpylä, P. J., & Brandenburg, A. 2009, *ApJ*, 699, 1059
 Käpylä, P. J., Korpi, M. J., & Brandenburg, A. 2008, *A&A*, 491, 353
 Mitra, D., Tavakol, R., Käpylä, P. J., & Brandenburg, A. 2010, *ApJ*, 719, L1
 Rädler, K.-H., & Bräuer, H.-J. 1987, *Astron. Nachr.*, 308, 101
 Rädler, K.-H., Wiedemann, E., Brandenburg, A., Meinel, R., & Tuominen, I. 1990, *A&A*, 239, 413
 Rheinhardt, M., & Brandenburg, A. 2010, *A&A*, 520, A28
 Schekochihin, A. A., Haugen, N. E. L., Brandenburg, A., et al. 2005, *ApJ*, 625, L115
 Schrunner, M., Rädler, K.-H., Schmitt, D., Rheinhardt, M., & Christensen, U. 2005, *Astron. Nachr.*, 326, 245
 Schrunner, M., Rädler, K.-H., Schmitt, D., Rheinhardt, M., & Christensen, U. R. 2007, *Geophys. Astrophys. Fluid Dyn.*, 101, 81
 Schrunner, M., Petitdemange, L., & Dormy, E. 2011, *A&A*, 530, A140
 Steenbeck, M., & Krause, F. 1969, *Astron. Nachr.*, 291, 49
 Stefani, F., & Gerbeth, G. 2003, *Phys. Rev. E*, 67, 027302